

THE AERODYNAMICS OF BLOWN FILM BUBBLE COOLING

V. Sidiropoulos and J. Vlachopoulos *

CAPPA-D
Dept. of Chemical Engineering,
McMaster University,
1280 Main St. West, Hamilton, ON, L8S 4L7
Canada

* Author to whom correspondence should be addressed

Abstract

Commercial blown film production is often limited by the rate of cooling that can be achieved in the production line. The flow of the cooling air (through narrow passages and around the curved bubble) is characterized by rather complex aerodynamics, including the Venturi and Coanda effects. Numerical simulations of cooling equipment for blown film bubbles have been carried out. It is shown that cooling efficiency is critically sensitive to varying airflow rates as well as the air ring design, as minor modifications cause large variations in cooling performance. Furthermore, even for a given design different setup of the adjustable parts can cause significant differences in the air-flow pattern and local cooling rates. In stacked-disk IBC equipment design, flow balancing is crucial for optimum operation.

Introduction

The air cooling system is an integral part of any blown film line. It greatly affects not only the heat transfer from the molten polymer film but also the formation and stability of the bubble. For most blown film bubbles the shape is primarily determined by mechanical manipulations and aerodynamics¹⁾. Several researchers²⁻⁶⁾ have examined the importance of heat transfer in film blowing modeling, as bubble cooling ultimately affects both production rates and final film properties.

Most conventional air-rings are dual orifice, though single orifice implementations are still used for high-stalk, HDPE bubbles. In a dual orifice setup, some of the air flow is injected through the lower orifice and flows between the cone and the bubble surface. It lowers the film temperature just enough for the film to become more durable. The rest of the cooling air is injected through the higher orifice onto the bubble surface. The operational setup of the air-ring determines the proportion of the cooling air that will flow through each orifice. Its adjustment is a delicate, mostly empirical process. Some air-rings also include a chimney and possibly more complex devices (like an IRIS diaphragm) to further redirect the cooling air and increase stability.

Two important aerodynamic phenomena are associated with the cooling airflow, namely the *Venturi* and *Coanda* effects⁷⁾. The well known **Venturi effect** is caused when a fluid flows through a constricted area: its speed increases and the pressure drops (figure 1). In film blowing, the bubble is pulled by the partial vacuum towards the walls of the air ring. The less known **Coanda effect**^{7,8)} occurs when a free jet emerges close to a surface: the jet tends to bend, “attach” itself and flow along the surface. The surface may be flat or curved and located inclined or offset to the jet (figure 2). The Coanda effect is more pronounced near curved surfaces, and blown film bubble surfaces with the cooling air impinging on them at an angle, offer the possibility of appearance of the Coanda effect.

Most modern air ring designs are quite complex, based on an abundance of design techniques and patents⁹⁻¹²⁾. Although air-rings offer some flexibility in adjusting some of the air flow settings, the adjustment itself is a rather empirical process usually performed by the line operators and perfected by experience. However, both Venturi and Coanda effects may be significantly influenced by only minor modifications in the original design and/or the operational set-up of an air-ring. This makes the tune-up of the air cooling system in blown film lines a rather unpredictable and awkward task.

As an addition to external air cooling, Internal Bubble Cooling (IBC) of blown film bubbles employs various mechanisms to exchange the internal air of the bubble. Naturally, this helps to increase the overall cooling of the film which would ultimately lead to increased production rates. IBC typically involves specifically designed equipment, engaged in exchanging the warm internal air with colder external air and also constantly circulating and mixing the internal air. In some cases the external air is chilled before being injected inside the bubble to maximize the cooling benefit. With IBC, the expected production rate improvement becomes increasingly important as die size and film layflat width increase. Production rate increases range from 20% for small bubbles (up to 8'' in die diameter) to as much as 80% for very large bubbles.

Although IBC systems decisively increase the production rate of numerous blown film bubbles, the expectations and excitement that was generated with the inception of the technology have only partially materialized. The reason appears to be the increased complexity of the technology and the introduction of many additional variables, which must be controlled.

Literature review

Isothermal models for film blowing (based on the balance of forces with the thin membrane approximation) started with the work of Petrie and Pearson¹³⁾. Petrie⁶⁾ introduced a non-isothermal rheological model. Ast²⁾ was the first one to attempt a solution of the energy equation. Wagner¹⁴⁾ and Cao and Campbell¹⁵⁾ introduced non-linear, non-isothermal, viscoelastic models. They realized the importance of the film temperature as a parameter in their modeling studies. Numerous other publications appeared¹⁶⁻²¹⁾ involving numerical modeling of the film blowing process, using Newtonian and viscoelastic constitutive equations. The main objective of these investigations was the determination of the bubble shape. It was shown that the effect of viscoelasticity is to decrease the ultimate bubble radius. However, this line of research did not produce any identifiable advances in blown film technology. In practice, the bubble shape is not determined by the polymer properties, but rather by mechanical manipulations and air-flow adjustments aimed at eliminating bubble instabilities and improving the end use of final film properties.

Some research has also been done on the experimental aspects of the problem. Kanai and White²²⁾ studied the effect of cooling rate on crystallization and Cao et al⁵⁾ measured the temperature gradients in the normal direction. In most of the previous studies heat transfer has been examined semi-

empirically without focusing on the actual transport mechanisms. Additionally, the cooling air imposed forces and their effects on the formation of the blown film bubble have been largely neglected.

Campbell et al⁴⁾ addressed the problem by introducing a full aerodynamic analysis (momentum and heat transfer) on the cooling air by using the method of superposition of stream functions as well as macro-balances of mass and energy. Wolf et al²³⁾ used the finite element method to solve the equations for jets impinging on a blown film bubble. Sidiropoulos et al²⁴⁾ used numerical simulation to compare the cooling profiles of single and dual orifice air-rings. Also, Hauck and Michaeli²⁵⁾ carried out an experimental investigation of film cooling and proposed an analytical model for the calculation of the heat transfer coefficients.

More recently, Akaike et al²⁶⁾ simulated a single orifice air ring and attempted to estimate how the cooling air affects the bubble formation in a coupled simulation. Sidiropoulos and Vlachopoulos studied the importance of the Venturi and Coanda effects⁷⁾, examined the sensitivity of air-ring performance on geometrical changes of the original design²⁷⁾ and looked at the performance and efficiency of internal bubble cooling (IBC) devices²⁸⁾. Wortberg and Spirgatis²⁹⁾ presented a detailed experimental study of the turbulent characteristics of the cooling airjet.

Theory

The Navier-Stokes equations are used to calculate the momentum transfer in the cooling air stream. Since the air flow is turbulent, the instantaneous velocities can be considered as the sum of a mean and a fluctuating velocity ($u_i=U_i+u'_i$). By taking the time-average of the Navier-Stokes equations (Reynolds averaging) most of the terms with fluctuating velocities vanish. The *Reynolds averaged* Navier-Stokes equations can be expressed as

$$\frac{\partial(\rho U_i)}{\partial t} + \frac{\partial(\rho U_i U_j)}{\partial x_j} = \frac{\partial}{\partial x_j} \left[\mu \left(\frac{\partial U_i}{\partial x_j} + \frac{\partial U_j}{\partial x_i} \right) - \left(\frac{2}{3} \mu \frac{\partial U_k}{\partial x_k} \right) \right] - \frac{\partial p}{\partial x_i} + \rho g_i + \frac{\partial}{\partial x_j} (-\rho \overline{u'_i u'_j}) \quad (1)$$

In equation (1) the effect of turbulence is included through the Reynolds stresses ($-\rho \overline{u'_i u'_j}$), which involve products of the velocity fluctuations.

The contribution of Reynolds stresses to the momentum balance is introduced through the concept of the *effective* viscosity (Boussinesq approximation). The Reynolds stresses are considered the product of a *turbulent* viscosity and the mean velocity derivatives. In contrast with molecular

viscosity, turbulent viscosity is not a fluid property and depends on local flow conditions. A variation of the so-called k-ε turbulent model (the RNG k-ε)³⁰ was used to reduce the number of unknowns (the three velocity components U₁, U₂, U₃, pressure and the velocity fluctuations) to the number of equations. The equations are the three components of the equation of conservation of momentum (1) and the equation of continuity (conservation of mass). The reduction of number of unknowns to the number of equations is known in the relevant literature as the turbulence *closure* problem.

Using the effective viscosity the mean momentum equation for two-dimensional flow becomes

$$\frac{\partial(\rho U_i)}{\partial t} + \frac{\partial(\rho U_i U_j)}{\partial x_j} = \frac{\partial}{\partial x_j} \left[\mu_{\text{eff}} \left(\frac{\partial U_i}{\partial x_j} + \frac{\partial U_j}{\partial x_i} \right) \right] - \frac{\partial p}{\partial x_i} \quad (2)$$

A similar to momentum transport equation (2) can be applied for the turbulent transport of energy, which in simplified form can be written as,

$$C_p \left(\frac{\partial(\rho T)}{\partial t} + \frac{\partial(\rho U_i T)}{\partial x_i} \right) = \frac{\partial}{\partial x_i} \left[\alpha \mu_{\text{eff}} C_p \frac{\partial T}{\partial x_i} + U_j \mu_{\text{eff}} \left(\frac{\partial U_i}{\partial x_j} + \frac{\partial U_j}{\partial x_i} \right) \right] \quad (3)$$

where α is the inverse of the turbulent Prandtl number.

A commercially available, adjustable dual-orifice air-ring (**Future Design Inc.**) was simulated using a finite volume computational method (**FLUENT**) in order to solve the system of differential equations. For each of the finite volumes, solution of equations (2) gives local values for pressure and velocities, while solution of equation (3) gives local values of temperature. The flow streamlines are calculated from the resulting velocity field. The heat transfer to the walls is calculated using the log-law formulation for the temperature derivative based on the analogy between heat and momentum transfer³¹.

Results and Discussion

External Bubble Cooling

The simulated air-ring is commercially available and manufactured by **Future Design Inc.** It is designed for bubbles with initial radius of 2 inches. A few grid topologies were examined, corresponding to various bubble shapes, cooling airflow rates and operating setups of the adjustable parts. Additionally,

minor geometric design modifications were performed to evaluate the heat transfer capability of the air rings. More details about the numerical simulations are available elsewhere³²).

Figure 3 shows the calculated streamlines around a typical HDPE high-neck type bubble shape. Different simulations are shown on the left and right sides of the figure for easy comparison. The left side shows the calculated streamlines for a high airflow rate (25 lt-of-air/s), while the right side shows the same for a medium airflow rate (12 lt-of-air/s). It is obvious that the increasing airflow rate drastically affects the character of the cooling air-jet. At the exit of the upper lip and for medium airflow rates, the air-jet bends and impinges on the curved film surface. This happens due to the Coanda effect, even though the jet was initially directed away from the film. For a higher airflow rate (left side of figure 3) this behavior is drastically altered. The Coanda effect initially forces the air-jet to initially attach to the external air-ring surface (stabilization cone). Above the air-ring, a second Coanda effect abruptly turns the air-jet towards the film surface, creating a large vortex. Further work showed that this transformation of the air-jet occurs suddenly at about the 18 lt-of-air/s mark.

Away from the air ring, a significant amount of ambient air is entrained and the jet slows down significantly. Near the frost line, the air velocity is usually one order of magnitude smaller than the velocity at the air-ring lips. Still the air jet remains attached to the film surface and closely follows its curvature. This is a common pattern for all the simulations that have been performed and is a direct result of the Coanda effect (cooling air streamlines always remain closely bound to the curved wall and follow its curvature).

Figure 4 shows a different set of simulations. The simulated bubble has a typical LLDPE bubble geometry. The two simulations presented in figure 4 (left and right side) correspond to different setups for the adjustable part of the air ring. The left side shows the streamline pattern for a low setup, while the right side depicts the flow when the air ring is adjusted at a higher position (2mm higher). The difference in the height of the adjusted part corresponds to approximately a full turn of the adjustable air-ring screw, an adjustment frequently performed by line operators. In both cases the airflow exhibits an overall apparent similarity. There are, however, significant differences in the area where the upper-orifice jet emerges.

The simulation for the low position setup shows that most of the air-flow is directed through the higher orifice. At the exit of the high-lip a strong Coanda effect is present creating a recirculating vortex.

The high position simulation shows more air directed through the lower orifice. While the majority of the air is still traveling through the higher orifice, the balance between the two flows is altered and the Coanda effect is absent from the high-lip area.

Figure 5 shows the calculated heat transfer coefficient profiles on the bubble surface (high and low air ring setup). In both cases an initial cooling peak is observed at the base of the air ring where the cold air traveling through the lower orifice is impinging on the very hot polymer film. As the lower-orifice air is traveling up the air-ring cone (tangentially to the bubble surface) its heat removal capability rapidly drops. A second cooling peak occurs after the rest of the air is injected through the upper lip. The lower-orifice cooling peak is larger for the high position setup. This was expected since more air is flowing through the lower orifice. On the other hand, the second peak is very small despite the fact that most of the air is still emerging through the higher orifice. Overall, the heat flux profile of the dual-orifice air ring at the high setup position is more similar with profiles obtained for single orifice air-rings^{23,24,26}.

The selective (and unpredictable) appearance of Coanda effects according to air-ring setup may explain what operators of blown film lines often encounter in production lines: frequently they manipulate the frost line and stabilize (or destabilize) the bubble by only slightly varying the adjustable air-ring setup. The presence of the Coanda effect greatly influences the heat transfer capability of the cooling air stream and the stability of the bubble.

Internal Bubble Cooling (IBC)

A typical IBC stacked disk configuration was also simulated. The selected IBC design is made for small bubbles with initial radius of 2 inches and would be installed in accordance with the external cooling equipment discussed above. The small size of the bubble and the equipment was specifically selected to illustrate the limitations of IBC on small bubbles. The bubble shape that was used was the LLDPE type shown in the external cooling simulations. The IBC slit stack that was employed in the simulation has a height equal to the height of the neck of the external air-ring (~8 cm). There are 4 slits in the IBC stack. The air is radially emerging from the 4 slits and impinges normally on the internal bubble surface. The slits have varying gaps to aid the homogenous distribution of the airflow.

Figure 6 compares the calculated streamline patterns for the original and a modified design³²) at the same airflow rate. The modified design uses an inlet annulus that is gradually reducing in gap as the

air flows upwards. Each contraction reduces the annular gap only by 10%. The predicted flow pattern for the modified IBC design is more balanced. Even though the top slits are slightly favored, substantial cooling air-jets emerge from all four slits. The cooling air impinges on the bubble surface at more points, creating more contact and recirculating patterns. Similar flow patterns were predicted for both higher and lower flow rates, indicating that the flow-balancing would be independent of airflow rate.

Figure 7 compares the calculated heat transfer coefficient profiles at the internal bubble surface (focusing in the impingement area where the differences are significant). The simulation of the modified design predicts four cooling peaks instead of two. This was expected since the form of the flow pattern (figure 6) suggests more impingement points. When compared to the original design, the cooling peaks have a smaller magnitude because the flow is further divided and more balanced. In the area above the direct impingement zone the heat transfer coefficient profiles for both original and modified design are indistinguishable. It is not immediately apparent which design is more cooling-efficient. For that, the calculated local heat transfer profiles were numerically integrated over the bubble surface area between the die lips and the frost-line. The integration at the simulated flow-rate indicates that the total internal heat flow induced by the original design is 38W, while the modified design generated a heat flow of 47W. This represents a 25% increase in the total cooling capacity of the modified IBC die. Taking into account the subtlety of the design modification, the cooling improvement is rather significant.

Concluding Remarks

The numerical simulation of the cooling airflow impinging on blown film bubbles provided a qualitative measure of the importance of the Venturi and Coanda effects as well as the performance sensitivity of cooling equipment in, often minor, design and setup modifications. The numerical results suggest that cooling performance (the limiting stage for higher production rates) is strongly influenced by the air-ring's design and setup as well as the optimization of any IBC equipment.

Acknowledgements

The authors would like to acknowledge Robert Krycki of **Future Design Inc.** for providing the commercial air-ring designs used in this work and many helpful discussions.

Nomenclature

C_p :	specific heat	u' :	fluctuating velocity
g :	gravitational acceleration	α :	inverse turbulent Prandtl number (1/Pr)
k :	turbulent kinetic energy	ε :	turbulent energy dissipation rate
p :	pressure	μ :	molecular viscosity
T :	temperature	μ_{eff} :	effective (total) viscosity
t :	time	ρ :	density
U :	average velocity	τ_{ij} :	stress tensor
u :	instantaneous velocity		

References

1. Kurtz, S. J.: Int. Polym. Proc., **10**, 148 (1995)
2. Ast, W.: Ph.D. thesis, IKT Stuttgart (1976).
3. Butler, T. I., Patel, R., Lai, S., and Spuria, J. E.: TAPPI Proceed., 13 (1993)
4. Campbell, G.A., Obot, N.T., and Cao, B.: Polym. Eng. Sci., **32**, 751 (1992)
5. Cao, B., Sweeney, P., and Campbell, G. A.: J. Plast. Film Sheet., **6**, 117 (1990)
6. Petrie, C. J. S.: AIChE J., **21**, 275 (1975)
7. Sidiropoulos, V., and Vlachopoulos, J.: Int. Polym. Proc., **15**, 40 (2000)
8. Bourque, C., and Newman, B. C.: Aeron. Quart., **11**, 201 (1960)
9. US Patent, 4479766 (1984), Planeta, M.
10. Canadian Patent, 1294100 (1992), Cole, R. J.
11. US Patent, 4373273 (1983), Church, R.
12. Knittel, R.R., and DeJonghe, J.: "Film Extrusion Manual: Blown Film Cooling Systems", 261, TAPPI press (1992)
13. Pearson, J. R. A., and Petrie C. J. S.: J. Fluid Mech., **40**, 1 (1970)
14. Wagner, M. H.: Ph.D. thesis, IKT Stuttgart (1976)

15. Cao, B., and Campbell, G. A.: *AIChE J.*, **36**, 420 (1990)
16. Luo, X.L. and Tanner, R.I.: *Polym. Eng. Sci.*, **25**, 620 (1985)
17. Liu, C.C., Bogue, D.C. and Spruiell, J. E.: *Intern. Polym. Proc.*, **10**, 230 (1995)
18. André, J. M., Agassant, J. F., Demay, Y., Haudin, J. M., and Monasse, B.: *Intern. J. Form. Proc.*, **1**, 187 (1998)
19. Agassant, J. F., Avenas, P., Sergent, J. P., and Carreau, P. J.: *Polymer Processing: Principles and Modelling*, Hanser Publishers, NY (1991)
20. Sidiropoulos, V., Tian, J.J., and Vlachopoulos, J.: *J. Plast. Film Sheet.*, **12**, 107 (1996)
21. Tanner, R. I.: *Engineering Rheology*, Oxford University Press, Oxford, UK (2000)
22. Kanai, T., and White, J.: *Polym. Eng. Sci.*, **24**, 1184 (1984)
23. Wolf, D., Feron, B., and Wortberg, J.: *Intern. Polym. Proc.*, **12**, 38 (1997)
24. Sidiropoulos, V., Wood, P. E., and Vlachopoulos, J.: *J. Reinf. Plast. Comp.*, **18**, 529 (1999)
25. Hauck, J. and Michaeli, W.: *Proceed. SPE ANTEC*, Atlanta, 123, (1998)
26. Akaike, O., Tsuji, T., and Nagano, Y.: *Intern. Polym. Proc.*, **14**, 168 (1999)
27. Sidiropoulos, V., and Vlachopoulos, J.: *Polym. Eng. Sci.*, **40**, 1611 (2000)
28. Sidiropoulos, V., and Vlachopoulos, J.: *Int. Polym. Proc.*, **16**, 48 (2001)
29. Wortberg, J. and Spirgatis, J.: 18th Annual Meeting of Polym. Proc. Soc., Guimaraes, Portugal (2002)
30. Fluent Inc., "Fluent Manual", Release 5.5 (1998)
31. Launder, B.E. and Spalding, D.B.: *Comp. Meth. Appl. Mech. Eng.*, **3**, 269 (1974)
32. Sidiropoulos, V., Ph.D. Thesis, McMaster University (2000)

List of Figures

Figure 1: Venturi effect: When a fluid flows through a constricted area its speed increases and the pressure drops	13
Figure 2: Coanda effect: A free jet emerging from a nozzle will tend to “attach” itself and flow along an inclined or offset nearby surface (flat or curved).....	13
Figure 3: Cooling air streamlines around a long neck (HDPE) bubble. left side: air flow 25 lt/s, right side: air flow 12 lt/s	14
Figure 4: Cooling air streamlines (air-flow 12 lt-of-air/s) around an LLDPE type blown film bubble for different operating setups of the adjustable air-ring. left side: low position setup, right side: high position setup	15
Figure 5: Heat transfer coefficient profile on the bubble surface at high and low positions of the adjustable air-ring (LLDPE type bubble shape).....	16
Figure 6: Stream-line comparison between the original and the modified IBC system (0.5 liters-of-air/s).....	17
Figure 7: Calculated heat transfer coefficient profiles for the original and the successive-gap-contractions design, as applied on the internal bubble surface for the same airflow rate (0.5 lt/s)	18

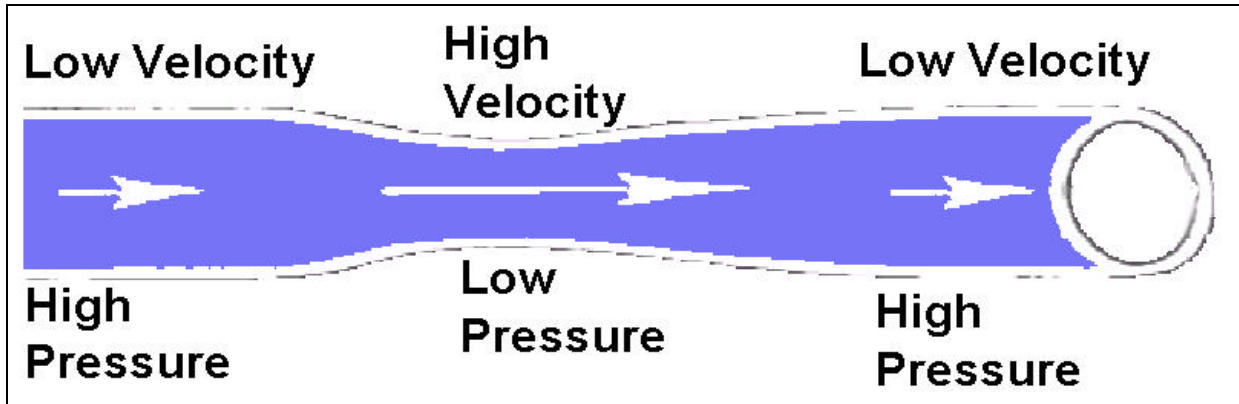


Figure 1: Venturi effect: When a fluid flows through a constricted area its speed increases and the pressure drops.

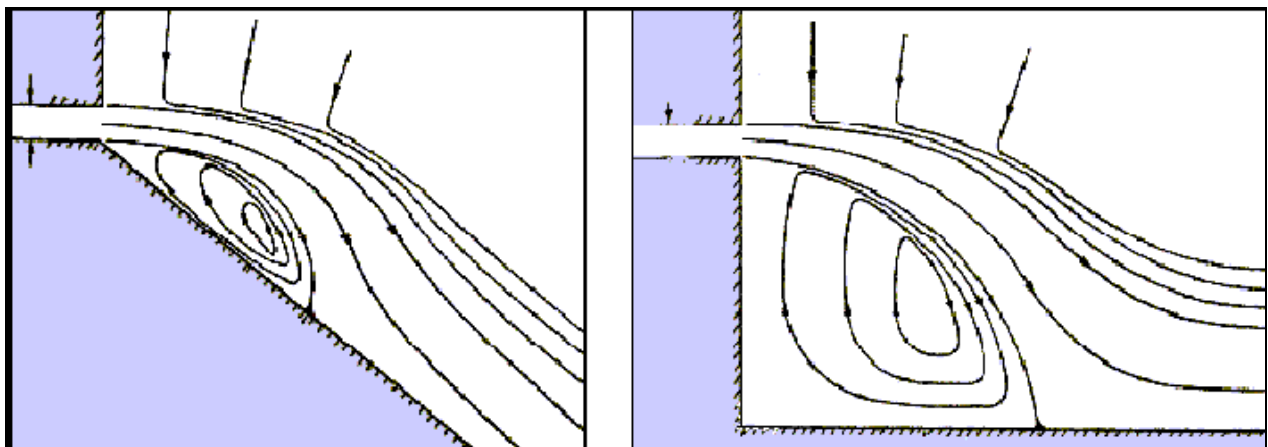


Figure 2: Coanda effect: A free jet emerging from a nozzle will tend to “attach” itself and flow along an inclined or offset nearby surface (flat or curved)

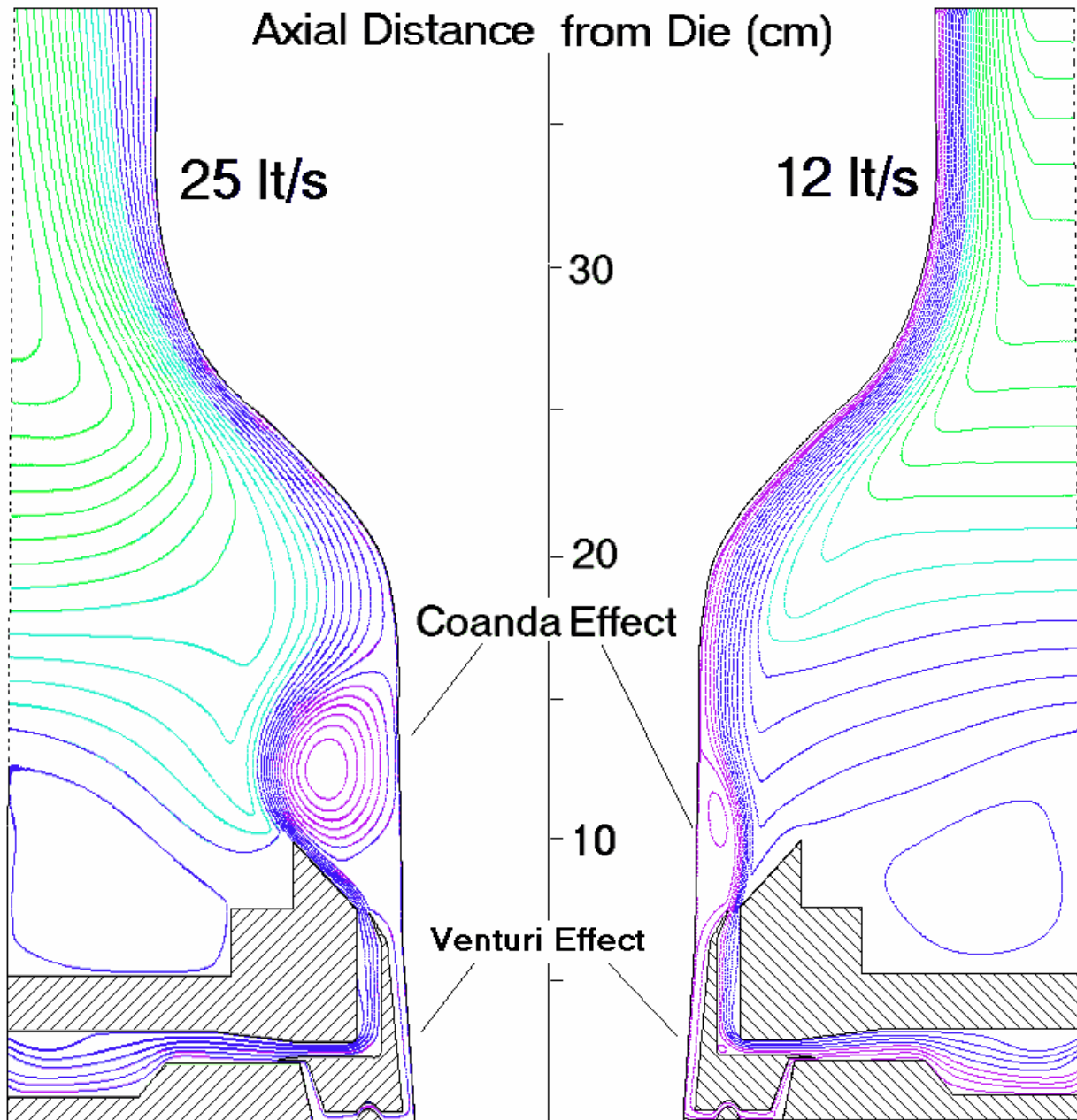


Figure 3: Cooling air streamlines around a long neck (HDPE) bubble.

left side: air flow 25 lt/s, right side: air flow 12 lt/s

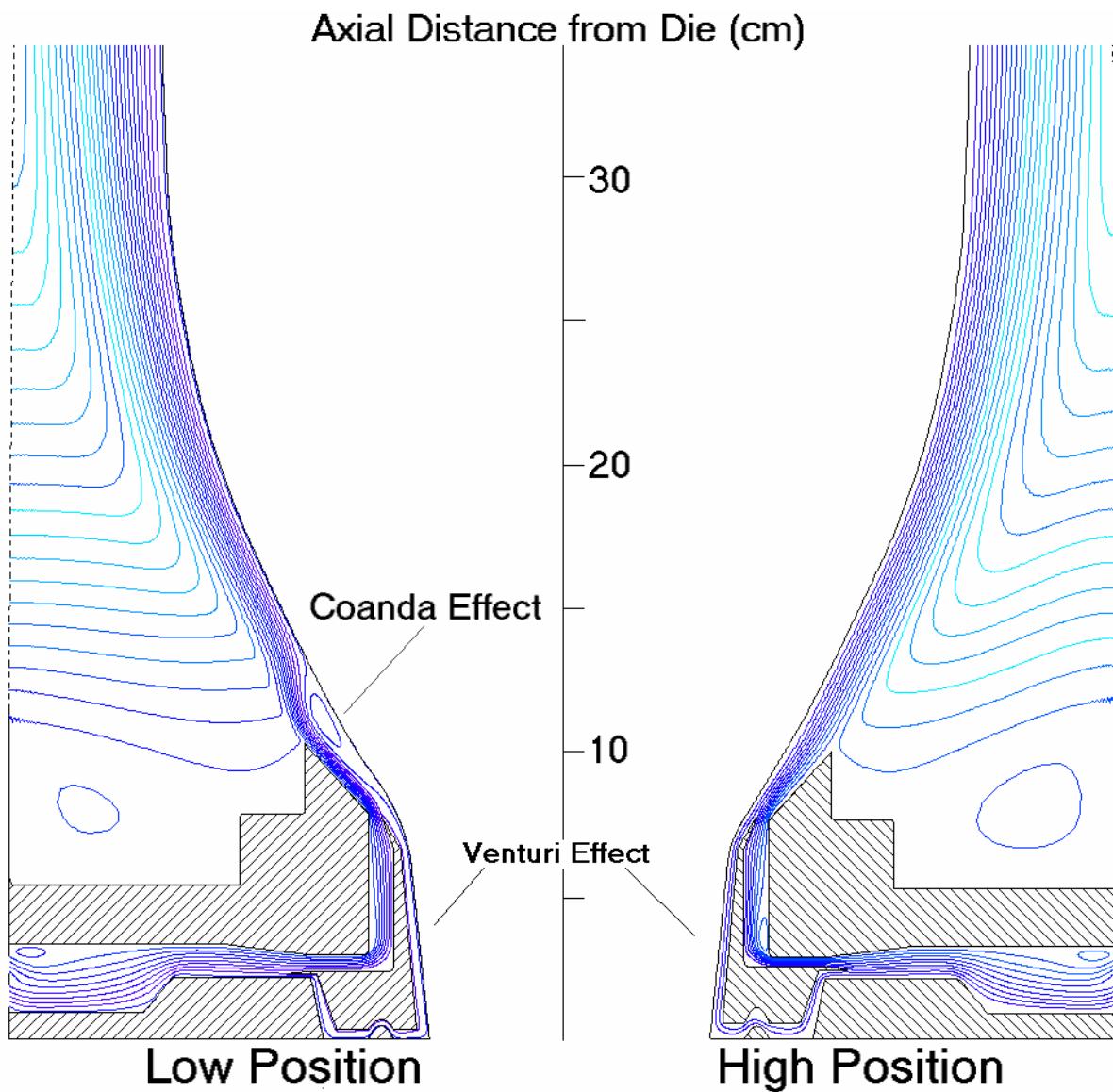


Figure 4: Cooling air streamlines (air-flow 12 lt-of-air/s) around an LLDPE type blown film bubble for different operating setups of the adjustable air-ring.
left side: low position setup, right side: high position setup

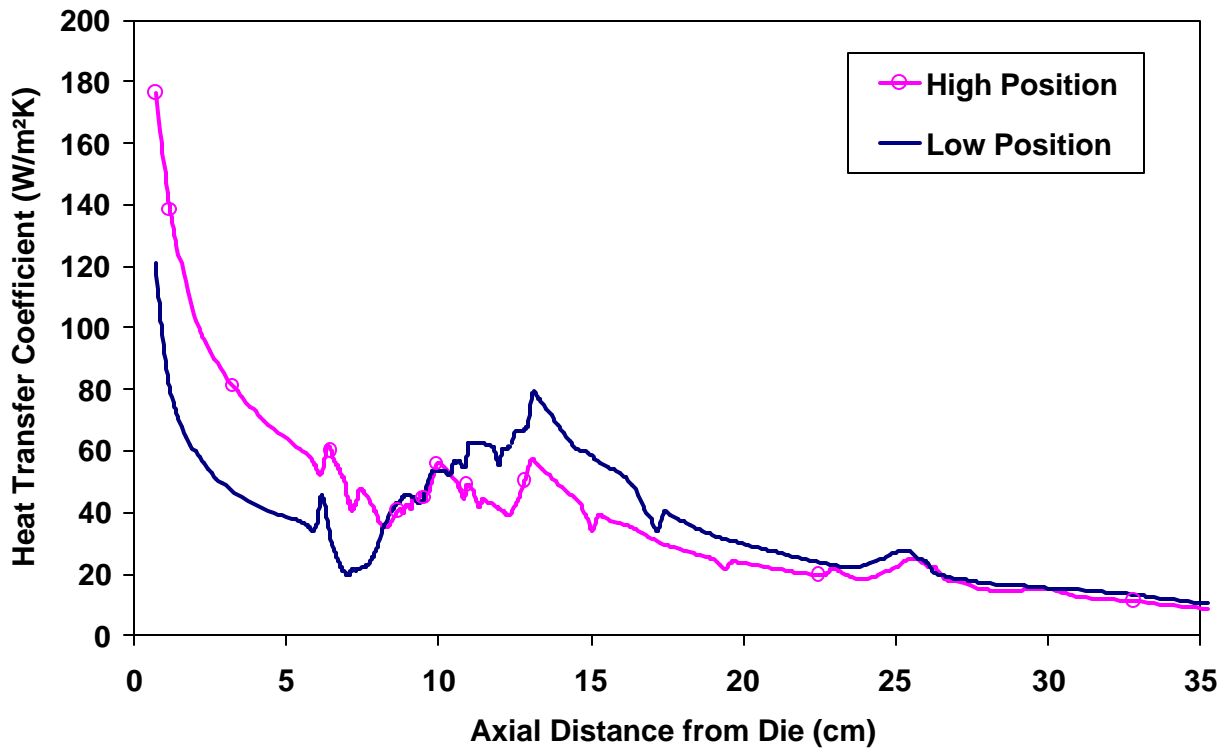


Figure 5: Heat transfer coefficient profile on the bubble surface at high and low positions of the adjustable air-ring (LLDPE type bubble shape)

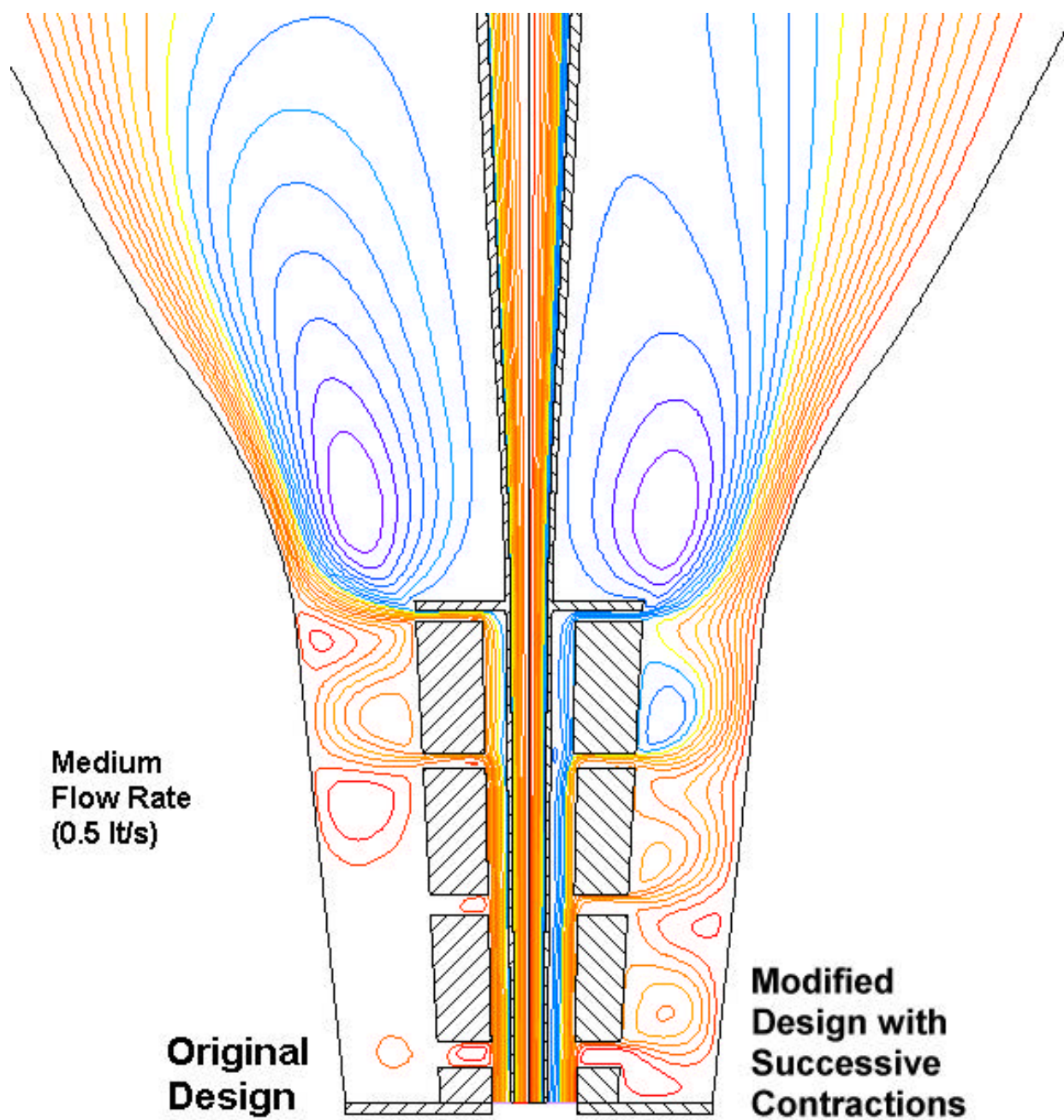


Figure 6: Stream-line comparison between the original and the modified IBC system
(0.5 liters-of-air/s)

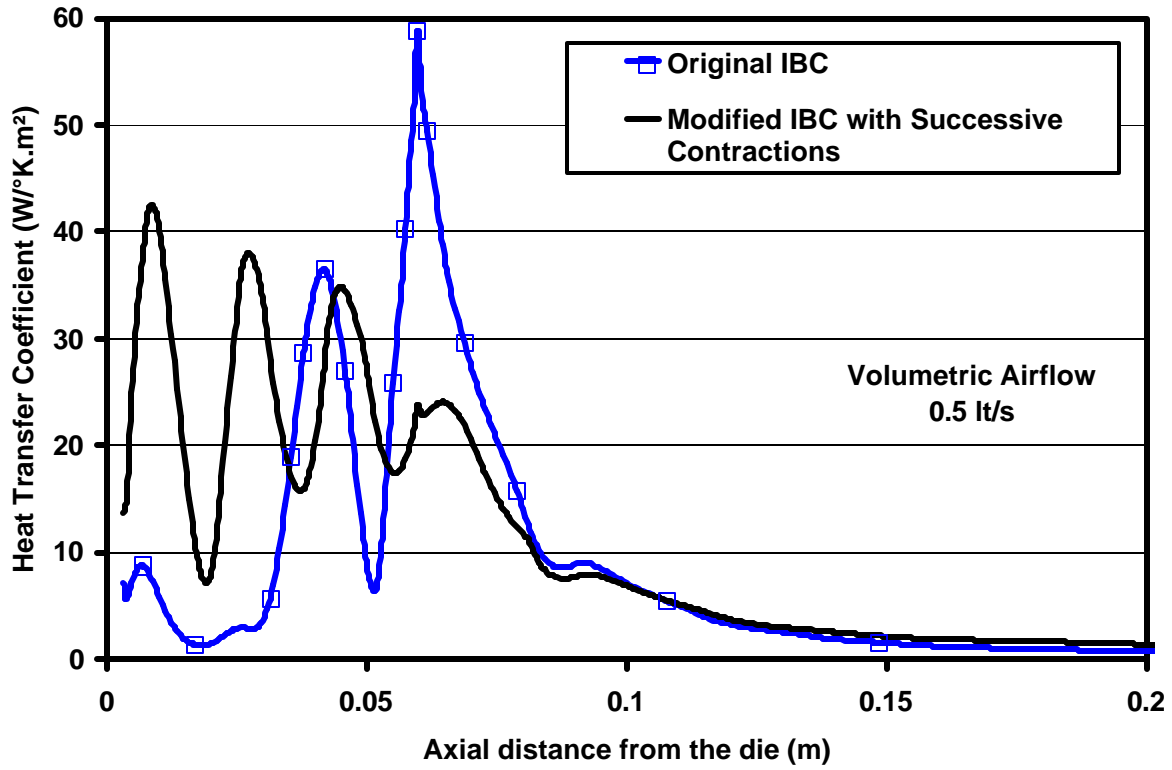


Figure 7: Calculated heat transfer coefficient profiles for the original and the successive-gap-contractions design, as applied on the internal bubble surface for the same airflow rate (0.5 lt/s)